Dynamical magnetic fields in heavy-ion collisions

Anping Huang,[1,2] Duan She,[3,4] Shuzhe Shi,[5,*] Mei Huang,[1,†] and Jinfeng Liao[2,‡]

[1]*School of Nuclear Science and Technology, University of Chinese Academy of Sciences, Beijing 100049, China*

[2]*Physics Department and Center for Exploration of Energy and Matter, Indiana University, 2401 N Milo B. Sampson Lane, Bloomington, Indiana 47408, USA*

[3]*Department of Modern Physics, University of Science and Technology of China, Anhui 230026, China*

[4]*Key Laboratory of Quark and Lepton Physics (MOE), Central China Normal University, Wuhan 430079, China*

[5]*Department of Physics and Astronomy, Stony Brook University, Stony Brook, New York 11794-3800, USA*

(Received 9 January 2023; accepted 8 February 2023; published 1 March 2023)

The magnetic fields in heavy-ion collisions are important ingredients for many interesting phenomena, such as the chiral magnetic effect, the chiral magnetic wave, the directed flow v_1 of D^0 mesons, and the splitting of the spin polarization of the $\Lambda/\bar{\Lambda}$. Quantitative studies of these phenomena, however, suffer from limited understanding of the dynamical evolution of these fields in the medium created by the collisions, which remains a critical and challenging problem. The initial magnetic fields from the colliding nuclei decay very fast in the vacuum but their lifetime could be extended through medium response due to electrically conducting quarks and antiquarks. Here we perform a detailed analysis of such medium effect on the dynamical magnetic fields by numerically solving Maxwell's equations concurrently with the expanding medium described by viscous hydrodynamics, under the assumption of negligible back reaction of the fields on the fluid evolution. Our results suggest a considerable enhancement of late time magnetic fields, the magnitude of which depends sensitively on the fireball expansion as well as the medium electric conductivity both before and during hydrodynamic stage.

DOI: 10.1103/PhysRevC.107.034901

I. INTRODUCTION

Ultrarelativistic heavy-ion collisions provide the opportunity to create quark-gluon plasma (QGP) and investigate its properties under extreme conditions in terms of temperatures, baryon densities, and more recently also magnetic fields and vorticity. There are very strong magnetic fields arising from the fast-moving ions in noncentral heavy-ion collisions, which can reach about $eB \sim m_\pi^2 \approx 10^{18}$ G in Au + Au collisions at the Relativistic Heavy Ion Collider (RHIC), and can be still an order of magnitude larger at the Larger Hadron Collider (LHC) [1–9]. Many interesting effects induced by such magnetic fields have been proposed and studied both theoretically and experimentally, such as the chiral magnetic effect, the chiral magnetic wave, the directed flow v_1 of D^0 mesons, the splitting of the spin polarization of the $\Lambda/\bar{\Lambda}$, etc. See recent reviews in, e.g., [10–16].

While the initial strength and spatial distribution of the magnetic fields at the beginning of a heavy ion collision can be accurately calculated, the subsequent dynamical evolution of such magnetic fields in the medium is rather poorly determined. If one only considers the field evolution in vacuum case, it is well known that the strength decays rapidly in time and the field lifetime at midrapidity can be estimated as $\tau_B \sim R_A/(\gamma\, v_z)$ which is about 0.06 fm for Au + Au collisions at 200 GeV [16] while it is about 0.005 fm for Pb + Pb collisions at 2.76 TeV. However, the lifetime of the in-medium magnetic field could be elongated due to the presence of the quark-gluon plasma in which the electrically charged quarks and antiquarks form a conducting medium with induction effect, as qualitatively demonstrated by various theoretical and numerical investigations [17–30]. A quantitative understanding of the dynamical evolution of magnetic fields, however, remains a key challenge.

Generally speaking, there are two different types of approaches: the "strong field" and "weak field" methods. In the strong field method, the influence of the electromagnetic fields on the medium evolution cannot be ignored and thus need to be taken into account for describing the medium. The most representative example is magnetohydrodynamics (MHD). In an ideal MHD with infinite conductivity, the magnetic field obeys the frozen flux (or Alfven) theorem and can therefore be represented simply in time [31,32] for a Bjorken flow, i.e., $B(\tau) = B_0\, \tau_0/\tau$, where B_0 is the initial magnetic field at time τ_0. Numerical efforts were developed in [33,34] by using the improved version of ECHO-QGP to simulate the evolution of electromagnetic fields in heavy-ion collisions by solving the relativistic ideal MHD equations with the assumption of

*shuzhe.shi@stonybrook.edu
†huangmei@ucas.ac.cn
‡liaoji@indiana.edu

infinite electrical conductivity of the plasma and ideal hydro behavior of the medium without dissipative effects. These analyses show that the medium effect would indeed slow down the decay of the magnetic field and hence enlarge its lifetime. However, given the strongly coupled nature of the quark-gluon plasma, it is difficult to imagine that the electric conductivity would be very large. In fact, lattice simulations would suggest a rather limited QGP electric conductivity.

In the weak field method, one assumes that the effect of the medium on electromagnetic fields must be accounted for while the back reaction of electromagnetic fields on the medium is negligible. In this approach, the medium evolution can be described by usual viscous hydrodynamics without electromagnetic fields and the evolution of the electromagnetic fields can be derived from Maxwell's equations by including the responses from the medium via, e.g., induction currents. Several previous theoretical and numerical works adopted this method; see, e.g., [7,8,35–42]. These studies also clearly demonstrated the medium response effect that can help extend the lifetime of magnetic fields, but often suffer from various unrealistic approximations, e.g., constant conductivity, static medium, one-dimensional Bjorken expansion only, infinite transverse medium, etc.

Quantitatively understanding the dynamical evolution of magnetic fields requires a more realistic hydrodynamic background, a more realistic QGP conductivity, a proper treatment of the full space-time dependence of the fields, as well as a careful analysis of the per-hydro nonequilibrium stage. In this work, we make an attempt at address these issues based on the weak field method through numerically solving concurrently the viscous hydrodynamics for the medium and Maxwell's equations for the electromagnetic fields. To be specific, let' us take the $\sqrt{s_{\rm NN}} = 200$ GeV Au + Au collisions as an example to demonstrate the developed framework. The full evolution includes three different stages in our framework. The first stage is the initial stage of time interval $\tau = 0.0$–0.1 fm, which may be gluon dominated with few quarks. At this time there would be no medium response and the electromagnetic fields are assumed to evolve in vacuum. The second stage is the pre-equilibrium stage of time interval $\tau = 0.1$–0.4 fm where the system is undergoing Bjorken expansion. While substantial numbers of quarks and antiquarks emerge in this stage, they may or may not be close to thermal equilibrium yet. Since there is no clear answer for the electric conductivity in such a nonequilibrium case, we will test several plausible assumptions for the preequilibrium effective electric conductivity, such as the zero model, constant model, and linear model. The third stage is the hydrodynamic stage for time $\tau \geqslant 0.4$ fm, in which the QGP medium is assumed to have thermal conductivity, and several scenarios for the conductivity will also be tested. A more detailed description of our framework will be presented later.

The rest of this paper is organized as follows. In Sec. II, the analytical solution and the numerical algorithm of Maxwell's equations in the static QGP scenario are briefly reviewed, with certain new results for dynamic magnetic fields under static QGP with space-time-dependent conductivity. In Sec. III, the dynamical evolution of magnetic fields in dynamically expanding QGP is studied and the results are compared for different models of both thermal and preequilibrium conductivities as well as for different choices of hydrodynamic backgrounds. Finally we conclude in Sec. IV. A number of relevant technical details are also included in several appendices: Appendix A presents the external electric and magnetic fields in heavy-ion collision as solutions of Eq. (11); Appendix B introduces Yee's grid algorithm for solving the Maxwell's equations; Appendix C briefly reviews the Levi-Civita tensor and electromagnetic tensor in Milne space used for the expanding case; Appendix D discusses the difference of the velocity in Milne space and Minkowski space.

II. DYNAMICAL MAGNETIC FIELD IN A STATIC QGP

The covariant Maxwell equations are

$$\partial_\mu F^{\mu\nu} = J^\nu, \quad \partial_\mu \widetilde{F}^{\mu\nu} = 0, \tag{1}$$

where $\widetilde{F}^{\mu\nu} = \frac{1}{2}\epsilon^{\mu\nu\alpha\beta}F_{\alpha\beta}$ is a dual tensor of the electromagnetic field tensor $F^{\mu\nu} = \partial^\mu A^\nu - \partial^\nu A^\mu$. Using the relations $B^i = -\frac{1}{2}\epsilon^{ijk}F_{jk} = \widetilde{F}^{i0}$, $E^i = F^{i0}$, $F^{ij} = \epsilon^{ijk}B_k$, the covariant Maxwell equations (1) can be rewritten in the familiar form

$$\begin{aligned} \nabla\cdot\mathbf{E} &= J^0, \\ \nabla\cdot\mathbf{B} &= 0, \\ \partial_t\mathbf{E} &= \nabla\times\mathbf{B} - \mathbf{J}, \\ \partial_t\mathbf{B} &= -\nabla\times\mathbf{E}. \end{aligned} \tag{2}$$

The first two equations are the constraint equations, while the last two equations the dynamical equations of the electromagnetic fields. The latter can be used to derive the electric and magnetic fields at the next time step. In a static medium, the current J^0 and $\mathbf{J}$ can expanded as

$$J^0 = J^0_{\rm s}, \quad \mathbf{J} = \sigma\mathbf{E} + \sigma_\chi\mathbf{B} + \mathbf{J}_{\rm s}, \tag{3}$$

with σ and σ_χ respectively being the electric and chiral conductivities of QGP. J^0_s and $\mathbf{J}_s$ are the source contributions from the fast moving protons in the colliding nuclei. They can be written as

$$J^0_{\rm s} = e\sum_i \delta(\mathbf{x}_\perp - \mathbf{x}'_{\perp,i})\delta(z - z'_i - \beta t), \tag{4}$$

$$\mathbf{J}_{\rm s} = e\sum_i \beta\hat{z}\,\delta(\mathbf{x}_\perp - \mathbf{x}'_{\perp,i})\delta(z - z'_i - \beta t). \tag{5}$$

From the above Maxwell equations (2), we can construct the corresponding wave equations for the electric and magnetic fields,

$$\begin{aligned} &\left(\nabla^2 - \partial_t^2 - \sigma\,\partial_t\right)\mathbf{E} - \sigma_t\mathbf{E} + \sigma_\chi\nabla\times\mathbf{E} \\ &\quad = \sigma_{\chi,t}\,\mathbf{B} + \partial_t\mathbf{J}_{\rm s} + \nabla J^0_{\rm s}, \\ &\left(\nabla^2 - \partial_t^2 - \sigma\,\partial_t\right)\mathbf{B} + (\nabla\sigma_\chi)\times\mathbf{B} + \sigma_\chi\nabla\times\mathbf{B} \\ &\quad = -(\nabla\sigma)\times\mathbf{E} - \nabla\times\mathbf{J}_{\rm s}, \end{aligned} \tag{6}$$

where we have used the notations $\sigma_t = \partial_t\sigma$, $\sigma_{\chi,t} = \partial_t\sigma_\chi$.

A. Analytical solution of Maxwell equations at constant conductivities

It is possible to analytically solve the Maxwell equations (2) or (6), when the electric and chiral conductivity are all constant for space-time [35,38–40]. In such a case, the wave equation (6) can be simplified as

$$\begin{aligned}\left(\nabla^2-\partial_t^2-\sigma\partial_t\right)\mathbf{E}+\sigma_\chi\nabla\times\mathbf{E}&=\partial_t\mathbf{J}_{\rm s}+\nabla J_{\rm s}^0,\\ \left(\nabla^2-\partial_t^2-\sigma\partial_t\right)\mathbf{B}+\sigma_\chi\nabla\times\mathbf{B}&=-\nabla\times\mathbf{J}_{\rm s}.\end{aligned}\tag{7}$$

Adopting the cylindric coordinate, its analytical solution is found to be [35,38–40]

$$\begin{aligned}B_\phi&=\frac{Q}{4\pi}\frac{v\gamma x_T}{\Delta^{3/2}}\left(1+\frac{\sigma v\gamma}{2}\sqrt{\Delta}\right)e^A,\\ B_r&=-\sigma_\chi\frac{Q}{8\pi}\frac{v\gamma^2x_T}{\Delta^{3/2}}[\gamma(vt-z)+A\sqrt{\Delta}]e^A,\\ B_z&=\sigma_\chi\frac{Q}{8\pi}\frac{v\gamma}{\Delta^{3/2}}\left[\gamma^2(vt-z)^2\left(1+\frac{\sigma v\gamma}{2}\sqrt{\Delta}\right)\right.\\ &\quad\left.+\Delta\left(1-\frac{\sigma v\gamma}{2}\sqrt{\Delta}\right)\right]e^A,\\ E_\phi&=\sigma_\chi\frac{Q}{8\pi}\frac{v^2\gamma^2x_T}{\Delta^{3/2}}[\gamma(vt-z)+A\sqrt{\Delta}]e^A,\\ E_r&=\frac{Q}{4\pi}\left\{\frac{\gamma x_T}{\Delta^{3/2}}\left(1+\frac{\sigma v\gamma}{2}\sqrt{\Delta}\right)\right.\\ &\quad\left.-\frac{\sigma}{vx_T}e^{-\sigma(t-z/v)}\left[1+\frac{\gamma(vt-z)}{\sqrt{\Delta}}\right]\right\}e^A,\\ E_z&=\frac{Q}{4\pi}\left\{-e^A\frac{1}{\Delta^{3/2}}\left[\gamma(vt-z)+A\sqrt{\Delta}+\frac{\sigma\gamma}{v}\Delta\right]\right.\\ &\quad\left.+\frac{\sigma^2}{v^2}e^{-\sigma(t-z/v)}\Gamma(0,-A)\right\},\end{aligned}\tag{8,9}$$

where $\Delta\equiv\gamma^2(vt-z)^2+x_T^2$, $A\equiv(\sigma v\gamma/2)[\gamma(vt-z)-\sqrt{\Delta}]$, and $\Gamma(0,-A)$ is the incomplete gamma function defined as $\Gamma(a,z)=\int_z^\infty dt\,t^{a-1}e^{-t}$.

As noted above, such an analytical solution is based on the precondition that the electric and chiral conductivities are space-time independent. Such a condition is not satisfied by the rapidly expanding medium form in the heavy-ion collision. It seems unrealistic to analytically solve the wave equations (6) or the Maxwell equations (2) when the conductivities are space-time dependent. Further investigatin of the realistic dynamical evolution of the electromagnetic field in heavy-ion collisions calls for numerical calculations.

B. Numerical method to solve Maxwell equations

Numerically solving the Maxwell equations (2) might be unstable, due to the Dirac delta functions in the source term. Therefore, we will adopt the method established by McLerran and Skokov [7]. In this method, the electric and magnetic fields are separated into two pieces, i.e.,

$$\mathbf{E}=\mathbf{E}_{\rm ext}+\mathbf{E}_{\rm int},\quad \mathbf{B}=\mathbf{B}_{\rm ext}+\mathbf{B}_{\rm int}.\tag{10}$$

The subscript "*ext*" denotes the external part which originated by the source contribution from the fast moving charge particles in heavy-ion collisions, whereas "*int*" refers to the induced electromagnetic fields generated in the created quark-gluon plasma (QGP). Then the Maxwell equations (2) under static medium now can been split into two parts. For the "external" part,

$$\begin{aligned}\nabla\cdot\mathbf{E}_{\rm ext}&=J_{\rm s}^0,\\ \partial_t\mathbf{E}_{\rm ext}&=\nabla\times\mathbf{B}_{\rm ext}-\mathbf{J}_{\rm s},\\ \nabla\cdot\mathbf{B}_{\rm ext}&=0,\\ \partial_t\mathbf{B}_{\rm ext}&=-\nabla\times\mathbf{E}_{\rm ext}.\end{aligned}\tag{11}$$

There is an analytical solution to this set of equations, which represent the electric and magnetic fields induced by the fast moving charged particles. Details can be found in Appendix A. The "internal" part is

$$\begin{aligned}\nabla\cdot\mathbf{E}_{\rm int}&=0,\\ \partial_t\mathbf{E}_{\rm int}&=\nabla\times\mathbf{B}_{\rm int}-\sigma\left(\mathbf{E}_{\rm int}+\mathbf{E}_{\rm ext}\right)-\sigma_\chi(\mathbf{B}_{\rm int}+\mathbf{B}_{\rm ext}),\\ \nabla\cdot\mathbf{B}_{\rm int}&=0,\\ \partial_t\mathbf{B}_{\rm int}&=-\nabla\times\mathbf{E}_{\rm int}.\end{aligned}\tag{12}$$

We numerically solve this equation set to obtain the internal electric and magnetic fields in the medium at any time, and then the resulting dynamical electric and magnetic fields in heavy-ion collisions are obtained by adding the external and internal parts.

For numerical stability for the conductivity ranging from 0 to ∞ when solving Eq. (12), we chose Yee's algorithm [43], which belongs to the category of leapfrog algorithms. In Yee's algorithm, the computed fields **E** and **B** are staggered by half a step in space-time with respect to each other. More details about the algorithm of Eq. (12) are presented in Appendix B. The code package of this section is publicly available [44].

C. numerical results

In this subsection, we present the numerical results using the aforementioned numerical method. The simulation is performed using initial conditions of the electromagnetic field provided by event-averaged Monte Carlo–Glauber (MC-Glauber) simulation for Au + Au collisions at RHIC energy $\sqrt{s_{NN}}=200$ GeV and impact parameter $b=6$ fm. The velocity and Lorentz factor for both target and projectile can be estimated by $v^2=1-\gamma^{-2}$ and $\gamma=\sqrt{s_{NN}}/2m_p$. To explore the effect of conductivity, we parametrize the electric conductivity as the result of hot QCD medium being obtained in the lattice calculations [19] scaled by a factor (λ),

$$\sigma=\lambda\,\sigma_{\rm LQCD}=5.8\,\lambda\ \text{MeV}.\tag{13}$$

To test the stability of our program and investigate influence of the conductivity on the evolution of the magnetic field, the parameter is chosen as $\lambda=1$, 10, 100, and 1000. The chiral conductivity is [45]

$$\sigma_\chi=\left(\frac{e^2}{2\pi^2}N_c\sum_f q_f^2\right)\mu_5,\tag{14}$$

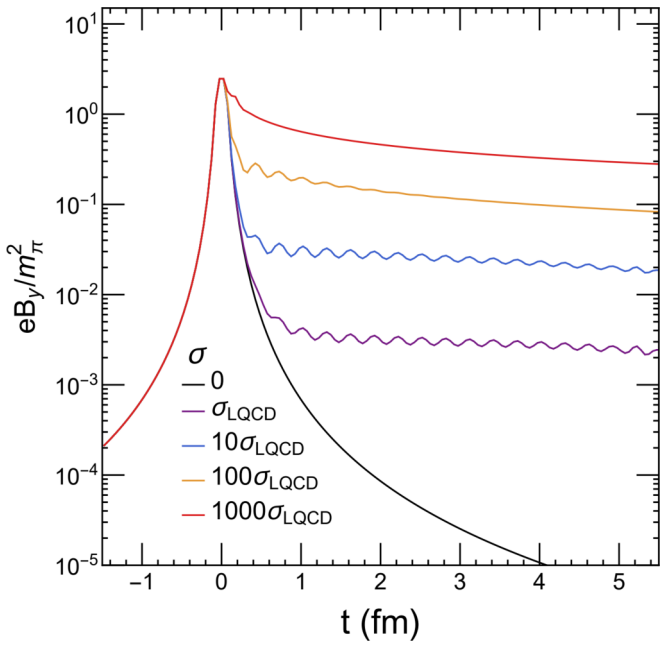

FIG. 1. The dynamical magnetic field in the static medium.

where μ_5 is the chiral chemical potential. Based on these inputs and the aforementioned method, we numerically solve the time evolution of the magnetic field in the origin $\mathbf{x} = 0$ as a function of the electric conductivity. Results are shown in Fig. 1, and are qualitatively consistent with McLerran and Skokov [7].[1] In our calculation, we took two values of the chiral chemical potential: an optimistic limit that $\mu_5 = 1$ GeV and a pessimistic limit that $\mu_5 = 0$. We find the difference between these two cases to be negligible.

The rapidly expanding conducting medium created in heavy-ion collisions is highly inhomogeneous. A realistic simulation requires a space-time-dependent electric conductivity. Meanwhile, quarks are not formed immediately after the initial collisions, and it takes finite time for the quark to equilibrate. One needs to pay special attention to the nontrivial time dependence of σ in the preequilibrium stage.

Herein, we test the influence of different components by choosing a couple of different models in the simulation. To explore the limits without transverse expansion and with the strongest one, we take two the Bjorken and Hubble models to estimate the time dependence of electric conductivity, $\sigma(t)$, i.e.,

$$\begin{aligned} \text{Bjorken:}\quad & \sigma(t) = \sigma_c \frac{T(t)}{T_c} = \sigma_c \frac{T_0}{T_c}\left(\frac{t_0}{t}\right), \\ \text{Hubble:}\quad & \sigma(t) = \sigma_c \frac{T(t)}{T_c} = \sigma_c \frac{T_0}{T_c}\left(\frac{t_0}{t}\right)^{\frac{1}{3}}. \end{aligned} \tag{15}$$

In our calculation, we take $T_0 = 3\,T_c$ and $\sigma_c = 10\,\sigma_{\rm LQCD}$. The spatial dependence is then modeled by assuming a homogeneous or Gaussian profile,

$$\begin{aligned} \text{homogeneous:}\quad & \sigma(t, \mathbf{x}) = \sigma(t), \\ \text{Gaussian:}\quad & \sigma(t, \mathbf{x}) = \sigma(t) e^{-\frac{x^2}{R_x^2} - \frac{y^2}{R_y^2} - \frac{z^2}{R_z^2}}, \end{aligned} \tag{16}$$

where the corresponding parameters in the Gaussian model are $R_x = R_A - b/2$, $R_y = \sqrt{R_A^2 - b^2/4}$, and $R_z = 3$ fm; $R_A = 6.38$ fm is the radius of Au; and $b = 6$ fm is the impact parameter. Finally, the effect of quark formation time is estimated by taking two limits: quarks at time $0 \leqslant t \leqslant t_0$ are not created at all, or rapidly created to the density at t_0. Correspondingly, the conductivity is parametrized as

$$\begin{aligned} \text{zero:}\quad & \begin{cases} \sigma(t) = 0, & t \leqslant t_0, \\ \sigma(t) \neq 0, & t_0 < t; \end{cases} \\ \text{nonzero:}\quad & \begin{cases} \sigma(t) = 0, & t \leqslant 0, \\ \sigma(t) = \sigma(t_0), & 0 < t \leqslant t_0, \\ \sigma(t) \neq 0, & t_0 < t. \end{cases} \end{aligned} \tag{17}$$

Here the $t_0 = 0.4$ fm is the start time of the hydro stage which is assumed as global equilibrium. The picture of these two cases is that the system is under the pre-equilibrium stage at time interval $0 < t < t_0$, and then the system is close to the equilibrium stage after time $t = t_0$. The difference is in the conductivity at the pre-equilibrium stage. Corresponding numerical results are shown in Fig. 2. It shows that $B(t)$ is very sensitive to the effective conductivity of the preequilibrium stage ($0 < t < t_0$) and the hydro stage ($t \geqslant t_0$). We note that in Ref. [37] the authors solve the Maxwell equation for a $\sigma(t)$ that is similar to our "zero" scenario, and in Fig. 2 we observe similar behavior for $B(t)$.

III. DYNAMICAL MAGNETIC FIELDS IN THE NONSTATIC QGP

A. The Maxwell equation in Milne space

It is convenient to use the Milne space for investigating the dynamic evolution of the electromagnetic field in the rapidly expanding QGP. The Maxwell equation can be expressed as

$$\hat{D}_\mu F_M^{\mu\nu} = J^\nu, \tag{18}$$

$$\hat{D}_\mu \widetilde{F}_M^{\mu\nu} = 0, \tag{19}$$

where the electromagnetic field tensor is marked with the subscript M to refer to Milne coordinates. The covariant derivative $\hat{D}_\mu$ acting on a tensor is expressed as $\hat{D}_\mu t^{\nu\rho} = \partial_\mu t^{\nu\rho} + \Gamma^\nu_{\lambda\mu} t^{\lambda\rho} + \Gamma^\rho_{\lambda\mu} t^{\nu\lambda}$, with affine connections $\Gamma^\rho_{\mu\nu} = (1/2) g^{\rho\sigma}(\partial_\nu g_{\sigma\mu} + \partial_\mu g_{\sigma\nu} - \partial_\sigma g_{\mu\nu})$. We adopt the metric convention to be $g_{\mu\nu} = \mathrm{diag}(1, -1, -1, -\tau^2)$. The dual tensor is $\widetilde{F}_M^{\mu\nu} = (1/2)\epsilon^{\mu\nu\rho\sigma} F^M_{\rho\sigma}$. Herein, the Levi-Civita tensor $\epsilon^{\mu\nu\rho\sigma}$ and the electromagnetic tensor are different from the case of Minkowski coordinate, and their explicit forms can be found in Appendix C. The currents are composed of normal currents, diffusion current, Ohm's law, and chiral magnetic effect (CME) current follows:

$$\begin{aligned} J^\mu &= J^\mu_{in} + J^\mu_{\rm s}, \\ J^\mu_{in} &= n\,u^\mu + d^\mu + \sigma\, F_M^{\mu\nu} u_\nu + \sigma_\chi \widetilde{F}_M^{\mu\nu} u_\nu. \end{aligned} \tag{20}$$

[1] We speculate that the difference in qualitative value is due to the fact that a different colliding system was considered in [7]. See also [41].

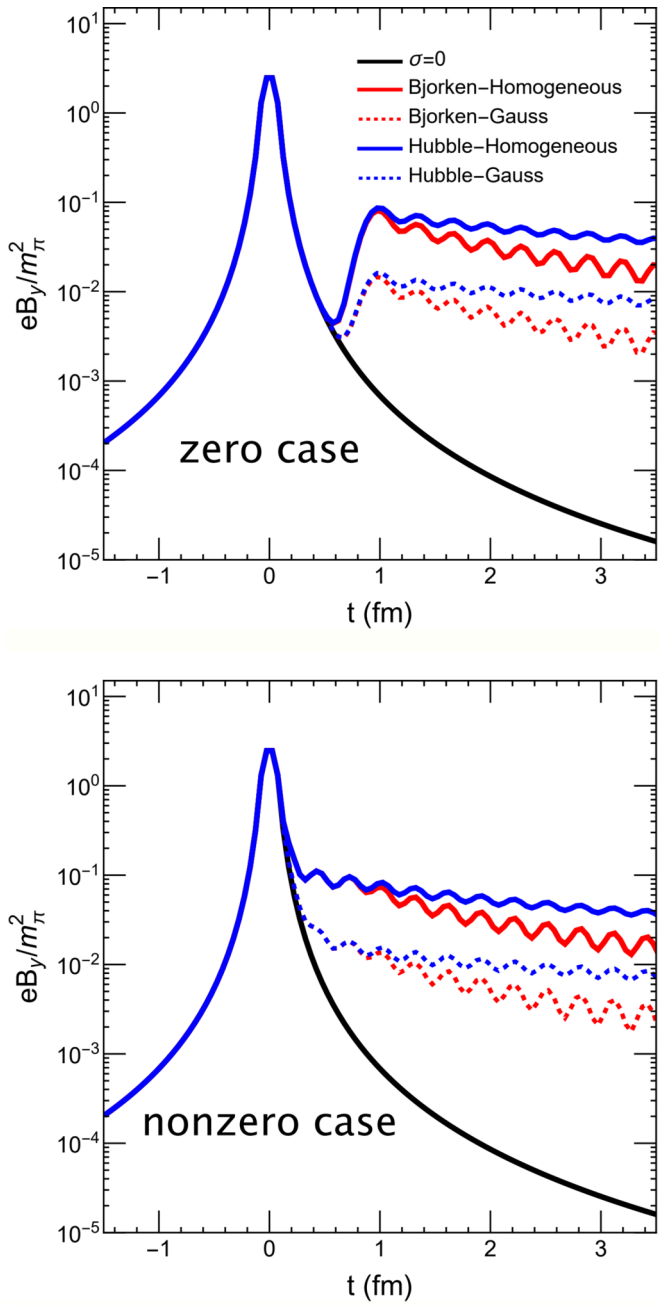

FIG. 2. Time dependence of the magnetic field along the out-of-plane direction. Upper and lower panels compare the effect of preequilibrium conductivity (17). In each plot, red and blue lines compare the temporal distribution (15), whereas solid and dashed lines compare the spatial distribution (16).

Herein, J^μ_{in} denotes the current in the medium and J^μ_s the source contributions from the fast moving charged particles in heavy-ion collisions; n is the charge number density and d^μ the diffusive current. We further denote electric and magnetic fields in the Milne space as

$$\widetilde{E}^i = F^{i0}_M, \quad \widetilde{B}^i = \widetilde{F}^{i0}_M, \tag{21}$$

with i being x, y, or η. The current in the medium can be further simplified as follows:

$$\begin{aligned}
J^\mu_{in} &= (J^\tau, J^x, J^y, J^\eta),\\
J^\tau &= n\,u^\tau + d^\tau + \sigma(\widetilde{E}^x u^x + \widetilde{E}^y u^y + \tau^2 \widetilde{E}^\eta u^\eta)\\
&\quad + \sigma_\chi(\widetilde{B}^x u^x + \widetilde{B}^y u^y + \tau^2 \widetilde{B}^\eta u^\eta),\\
J^x &= n\,u^x + d^x + \sigma(\widetilde{E}^x u^\tau + \tau \widetilde{B}^\eta u^y - \tau \widetilde{B}^y u^\eta)\\
&\quad + \sigma_\chi(\widetilde{B}^x u^\tau - \tau \widetilde{E}^\eta u^y + \tau \widetilde{E}^y u^\eta),\\
J^y &= n\,u^y + d^y + \sigma(\widetilde{E}^y u^\tau - \tau \widetilde{B}^\eta u^x + \tau \widetilde{B}^x u^\eta)\\
&\quad + \sigma_\chi(\widetilde{B}^y u^\tau + \tau \widetilde{E}^\eta u^x - \tau \widetilde{E}^x u^\eta),\\
J^\eta &= n\,u^\eta + d^\eta + \sigma\left(\widetilde{E}^\eta u^\tau + \frac{\widetilde{B}^y}{\tau} u^x - \frac{\widetilde{B}^x}{\tau} u^y\right)\\
&\quad + \sigma_\chi\left(\widetilde{B}^\eta u^\tau - \frac{\widetilde{E}^y}{\tau} u^x + \frac{\widetilde{E}^x}{\tau} u^y\right).
\end{aligned} \tag{22}$$

In order to facilitate the subsequent numerical calculations, let us further simplify the above Maxwell equations. From Eq. (18) and (19), one can get the evolution equations of the electric and magnetic fields as

$$\begin{aligned}
\partial_x \widetilde{E}^x + \partial_y \widetilde{E}^y + \partial_\eta \widetilde{E}^\eta &= J^\tau,\\
\partial_\tau(\tau\,\widetilde{E}^x) &= \partial_y(\tau^2 \widetilde{B}^\eta) - \partial_\eta \widetilde{B}^y - \tau\,J^x,\\
\partial_\tau(\tau\,\widetilde{E}^y) &= -\partial_x(\tau^2 \widetilde{B}^\eta) + \partial_\eta \widetilde{B}^x - \tau\,J^y,\\
\partial_\tau(\tau\,\widetilde{E}^\eta) &= \partial_x \widetilde{B}^y - \partial_y \widetilde{B}^x - \tau\,J^\eta;
\end{aligned} \tag{23}$$

$$\begin{aligned}
\partial_x \widetilde{B}^x + \partial_y \widetilde{B}^y + \partial_\eta \widetilde{B}^\eta &= 0,\\
\partial_\tau(\tau\,\widetilde{B}^x) &= -\partial_y(\tau^2 \widetilde{E}^\eta) + \partial_\eta \widetilde{E}^y,\\
\partial_\tau(\tau\,\widetilde{B}^y) &= \partial_x(\tau^2 \widetilde{E}^\eta) - \partial_\eta \widetilde{E}^x,\\
\partial_\tau(\tau\,\widetilde{B}^\eta) &= -\partial_x \widetilde{E}^y + \partial_y \widetilde{E}^x.
\end{aligned} \tag{24}$$

Now we can carry out the simulations with above equations (23) and (24), according to the aforementioned numerical method in Sec. II B. In the final numerical results, we will compute the electric and magnetic fields in Minkowski coordinates, which are Lorentz transformation of electric and magnetic fields in Milne coordinates by the following:

$$\begin{aligned}
E^x &= \cosh\eta\,\widetilde{E}^x + \sinh\eta\,\widetilde{B}^y,\\
E^y &= \cosh\eta\,\widetilde{E}^y - \sinh\eta\,\widetilde{B}^x,\\
E^z &= \tau\widetilde{E}^\eta,\\
B^x &= \cosh\eta\,\widetilde{B}^x - \sinh\eta\,\widetilde{E}^y,\\
B^y &= \cosh\eta\,\widetilde{B}^y + \sinh\eta\,\widetilde{E}^x,\\
B^z &= \tau\widetilde{B}^\eta.
\end{aligned} \tag{25}$$

B. Electric conductivity

The electric conductivity of QGP remains an open question. There are many works focusing on the electric conductivity in the hydro stage of QGP using theoretical calculations and simulations, but significantly different results are obtained. Here we briefly outline some of them in the fol-

lowing for further estimation of the reasonable region. First, results from different lattice QCD calculations can be different by an order of magnitude. They are listed as follows:

$$\begin{aligned}
&[17]\ \tfrac{\sigma}{T}|_{1.5<T/T_c<3} = 7C_{em} \approx 0.428,\\
&[18]\ \tfrac{\sigma}{T}|_{T/T_c\approx 1.5} = (0.4\pm 0.1)C_{em} = 0.0245 \pm 0.006,\\
&[19,20]\ \tfrac{\sigma}{T}|_{1.1T_c} = (0.201\text{–}0.703)C_{em} \approx (1.23\text{–}4.30)\times 10^{-2},\\
&\tfrac{\sigma}{T}|_{1.3T_c} = (0.203\text{–}0.388)C_{em} \approx (1.24\text{–}2.37)\times 10^{-2},\\
&\tfrac{\sigma}{T}|_{1.5T_c} = (0.218\text{–}0.413)C_{em} \approx (1.33\text{–}2.52)\times 10^{-2},
\end{aligned}$$

where the factor $C_{\rm em} = \sum_f e_f^2 \approx 0.06115$ for the three-flavor case, and e_f is the charge of a quark with flavor f.

Additionally, results from different theoretical calculations are also different. The hard thermal loop (HTL) calculation up to leading logarithm for high temperature QGP produces $\sigma/T = 11.8687 e \frac{{\rm Tr}_f(Q_e Q_V)}{g^4 \ln(1/g)} = 146.33(26.12)$ for $\alpha_s = 0.01(0.05)$ [23], where $Q_e = (2/3, -1/3, -1/3)$ for (u, d, s) and the numerical results are for $Q_V = Q_e$. Meanwhile, the leading order perturbative QCD calculation gives $\sigma/T \approx 5.98$ [29], whereas the dilute instanton-liquid model gives $\sigma/T \approx (0.46\text{–}1.39)C_{em} \approx (0.0281\text{–}0.0850)$ [27]. The transport model with relaxation time gives us an analytical representation (see, e.g., [25,46–49]),

$$\sigma = \sum_{f,\pm} \frac{g_f q_f^2 \tau_q}{6\pi^2 T} \int \frac{k^2 dk}{E_{k,f}^2} \frac{e^{-\frac{E_{k,f}\pm\mu}{T}}}{\left(e^{-\frac{E_{k,f}\pm\mu}{T}}+1\right)^2}, \tag{26}$$

where the $+$ $(-)$ sign indicates fermion (antifermion). One can estimate $\sigma/T = 0.007\text{–}0.026$ for $T = T_c - 5T_c$ with zero chemical potential.[2] Furthermore, the parton-hadron-string dynamics (PHSD) transport [28] approach finds that $\sigma/T \approx 0.0009 + 0.015(T - T_c)/T_c$. Finally, simulation using the microscopic relativistic transport model Boltzmann Approach to Multi-Parton Scatterings (BAMPS) [50] obtained $\sigma/T \approx (0.05\text{–}0.2)$.

Based on the above summary, we choose $\sigma/T = 0.1$ as a relatively reasonable value in our numerical simulation. We also take $\sigma/T = 100$ to explore the medium response in the large conductivity limit.

C. Numerical results

In this subsection, we present the simulate results of the electromagnetic field evolution in the no-static QGP. As mentioned before, the evolution of the medium formed in the relativistic heavy-ion collision, as well as that of the electromagnetic field, consists of three stages: initial ($\tau < 0.1$ fm), preequilibrium ($0.1 \leqslant \tau < 0.4$ fm), and hydro ($\tau \geqslant 0.4$ fm) stages. Our simulation will be arranged accordingly. The initial condition of the electromagnetic field is generated by two heavy nuclei moving toward each other. Then we solve the Maxwell's equations (23) and (24) and simulate the electromagnetic field evolution in the preequilibrium and hydro stages. In the pre-equilibrium stage, the QGP is assumed to expand as a Bjorken flow, and we explore three different models for the time dependence of the electrical conductivity. In the hydro stage, we take the hydro background from Bjorken flow, Gubser flow, and a realistic hydro profile from the MUSIC package [51–54]. The corresponding temperature and fluid velocity are produced by these three models. (See Appendix D for analytical forms of temperature and fluid velocity in the Bjorken and Gubser solutions.) These temperature and fluid velocity profiles are then read into the program and provide the background field to solve Maxwell's equations (23) and (24). In what follows, we will focus on the dynamical magnetic field at the center of the fireball [$\mathbf{x} = (0, 0, 0)$].[3] Herein, we focus on the case that the net number density (n) and the diffusive current density (d^μ) are set to zero, and their influence on the dynamic evolution of the magnetic field will be studied in our future work.

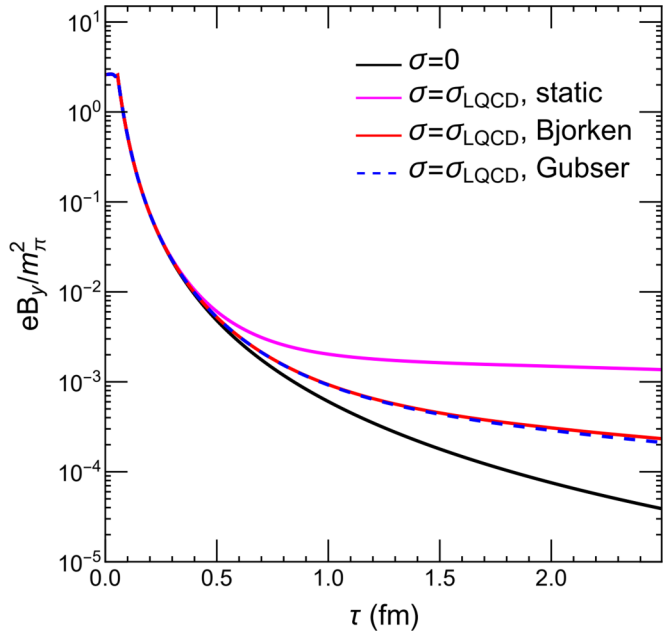

FIG. 3. The suppression effect of the longitudinal expansion of the medium.

1. *Suppression effect due to the longitudinal expansion of the medium*

We first study the evolution of magnetic field along the out-of-plane direction (eB_y) with three different backgrounds: a static medium, Bjorken flow, and Gubser flow. We take identical electric conductivities in these three different cases, i.e., $\sigma = 0$ for the initial stage, and $\sigma = \sigma_{\rm LQCD}$ for the preequilibrium and hydro stages. Results are shown in Fig. 3. We

[2] In this estimation, the relaxation time is $\tau_q = \frac{1}{5.1 T \alpha_s^2 \ln(\alpha_s^{-1})[1+0.12(2N_f+1)]}$, $g_f = 2\times 3$, the mass is the effective mass composed of the bare mass and thermal mass, and the coupling constant $\alpha_s(T) = \frac{6\pi}{(33-2N_f)\ln(T/\Lambda_T)}\left(1 - \frac{3(153-19N_f)}{(33-2N_f)^2}\frac{\ln[2\ln(T/\Lambda_T)]}{\ln(T/\Lambda_T)}\right)$, with $\Lambda_T = 200$ MeV.

[3] It is worth noting that we can generate the dynamic magnetic and electric fields at any given coordinate and the spatial distribution of electromagnetic fields at any time under our framework.

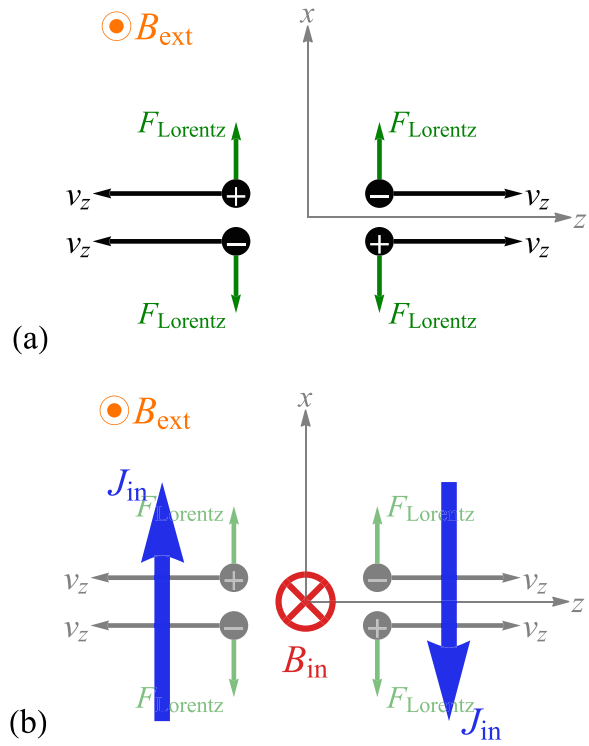

FIG. 4. Illustration of the suppression effect. (a) Lorentz force acting on in-medium charged particles due to the external magnetic field. (b) Induced electric currents due to the Lorentz force and their resulting induced magnetic field.

observe a suppression effect for the longitudinal expansion of the medium. The dynamical magnetic field was depressed in the Bjorken expansion and the Gubser expansion compared to the static case.

The reason for the suppression effect is illustrated in Fig. 4 and explained as follows. In the presence of a external magnetic field along the y axis, in-medium particles with positive (negative) at forward rapidity experience a Lorentz force pointing at the negative (positive) x direction, and vice versa for particles at backward rapidity. Collective motion of the charged particles, due to the Lorentz force, induces a clockwise circular current. It generates an induced magnetic field in the negative y direction and thereby weakens the external magnetic field.

2. *The dynamical magnetic field with realistic hydro background*

Now we move on to the realistic hydrodynamic background provided by numerical simulation using the MUSIC package [51–54]. We set $\sigma = 0$ at the initial stage, and we explore the medium responses to the magnetic field by choosing three different electric conductivity models in the preequilibrium stage and respectively setting the electric conductivity $\sigma = 0.1\,T$, $\sigma = \sigma_{\rm LQCD}$, and $\sigma = 100\,T$ in the hydro stage. The three models for the preequilibrium stage are (a) zero model that assumes vanishing conductivity, $\sigma(\tau, \mathbf{x}) = 0$; (b) constant model that assumes constant conductivity, which takes the value at the initial time of the hydro stage, $\sigma(\tau, \mathbf{x}) = \sigma(\tau = 0.4\ \text{fm}, \mathbf{x})$; and (c) linear model that the conductivity that grows linearly from zero to the value at the hydro initial time, $\sigma(\tau, \mathbf{x}) = (\tau/0.4\ \text{fm})\sigma(\tau = 0.4\ \text{fm}, \mathbf{x})$. We will assume that the temperature and velocity of the background flow in the preequilibrium stage follow the Bjorken flow.

Both hydro and electromagnetic field initial conditions are generated by event-averaged MC-Glauber simulation for $\sqrt{s_{NN}} = 200$ GeV AuAu collisions. For a more direct comparison of the response of different hydro profiles, we fix the magnetic field to be the one with impact parameter $b = 6$ fm, and vary the hydro background from 10–20% to 50–60% centrality classes.

Results for $\sigma = 0.1T$ in the hydro stage are presented in Fig. 5. The dynamical magnetic field is more sensitive to the electric conductivity model of the preequilibrium stage than to the hydro background. The dynamical magnetic fields in Bjorken, Gubser, and realistic backgrounds are almost the same except for the late time region where the magnetic field strength is very small. It means that the evolution of

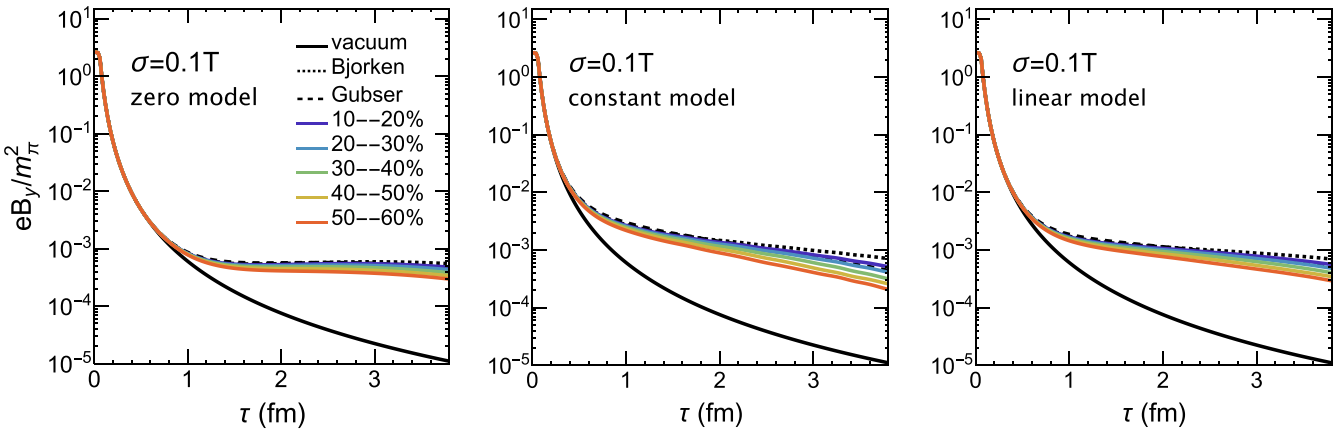

FIG. 5. Proper dependence of magnetic field along the out-of-plane direction at the center ($x = 0, y = 0, z = 0$) and with conductivity $\sigma = 0.1\,T$ in the hydro stage. Panels from left to right correspond to zero, linear, and constant models for the preequilibrium stage. Black solid curves represent the vacuum value, whereas dotted (dashed) curves take Bjorken (Gubser) flow as the background. Colored solid curves from purple to red are respectively for realistic hydro backgrounds in the 10–20% to 50–60% centrality classes.

TABLE I. The fit parameters of the fitted magnetic field Eq. (27) for electric conductivity $\sigma = 0.1\,T$ in the hydro stage with a different conductivity model in the preequilibrium stage.

	a_0	b_0	b_1	b_2	c_0	c_1	c_2	c_3
zero model	−8.848	−2.193	0.412	−0.207	0.0	13.074	−11.66	19.679
constant model	−21.693	−28.039	−148.773	−16.302	0	159.619	6.285	4.948
linear model	−10.177	−7.549	0.183	−0.299	0.351	36.926	−16.311	3.285

the y component of the magnetic field is dominated by the longitudinal expansion of the QGP, rather than the transverse expansion. We fit the magnetic field as a function of time with a parameterized function,

$$e\,B^y = e\,B^y_{\tau=0} \exp\left[a_0\, e^{\frac{b_0+b_1\tau+b_2\tau^2}{c_0+c_1\tau+c_2\tau^2+c_3\tau^3}}\right]. \tag{27}$$

Corresponding parameters in Table I are fit from the data of the MUSIC hydro background with centrality 40–50%.

Then we investigate the evolution of magnetic field with the constant conductivity $\sigma = \sigma_{\rm LQCD}$ in the hydro stage. Results are presented in Fig. 6, and parameter fit for 40–50% centrality range is listed in Table II. Given the constant conductivity, the influence of transverse expansion become negligible.

Finally, let us explore the response of a highly conductive plasma where the electric conductivity is 1000 times that in the hydro stage, i.e., $\sigma = 100\,T$. Results are shown in Fig. 7 and Table III. Compared with the results in Fig. 5, the late-time strength of the magnetic field is much greater, and it is more explicitly dependent on the choice of the conductivity model in the preequilibrium stage.

IV. CONCLUSION

To conclude, we have developed a framework to numerically simulate the dynamical magnetic fields in heavy ion collisions. This framework has allowed us to investigate the in-medium evolution of space-time-dependent magnetic fields on top of a variety of background medium evolution models for different scenarios of electric conductivities both in the thermal phase and in the pre-equilibrium stage. Our main findings can be summarized as follows.

(i) In the case of a static QGP, previous results assuming constant electric conductivity are reproduced and new results with more realistic space-time-dependent electric conductivity are obtained, demonstrating a robust medium response that extends the lifetime of the magnitude and that is sensitive to the values of the conductivity.

(ii) For an expanding QGP, we find a strong influence of the longitudinal expansion which considerably reduces the contributions from medium response and as a result leads to a much smaller magnetic fields as compared with the static case. On the other hand, the inclusion of transverse expansion in addition to the longitudinal expansion only affects the dynamical field evolution rather mildly.

(iii) The lifetime of the dynamical magnetic fields is strongly dependent on the medium conductivities in the thermal QGP. Choosing a conductivity value in the range implied by relevant lattice simulations would only lead to a limited medium enhancement of late time field strength.

(iv) More importantly, the lifetime is found to be particularly sensitive to, and mainly determined by, the nonequilibrium contribution from the early time partonic medium, as demonstrated by comparisons among the three different choices (zero model, constant model, and linear model). A considerable prehydro effective conductivity could significantly enhance the dynamical field strength.

Clearly, the main "bottleneck" for an accurate description of the dynamical magnetic fields is a better estimate of the effective conductivity for the preequilibrium stage, which in

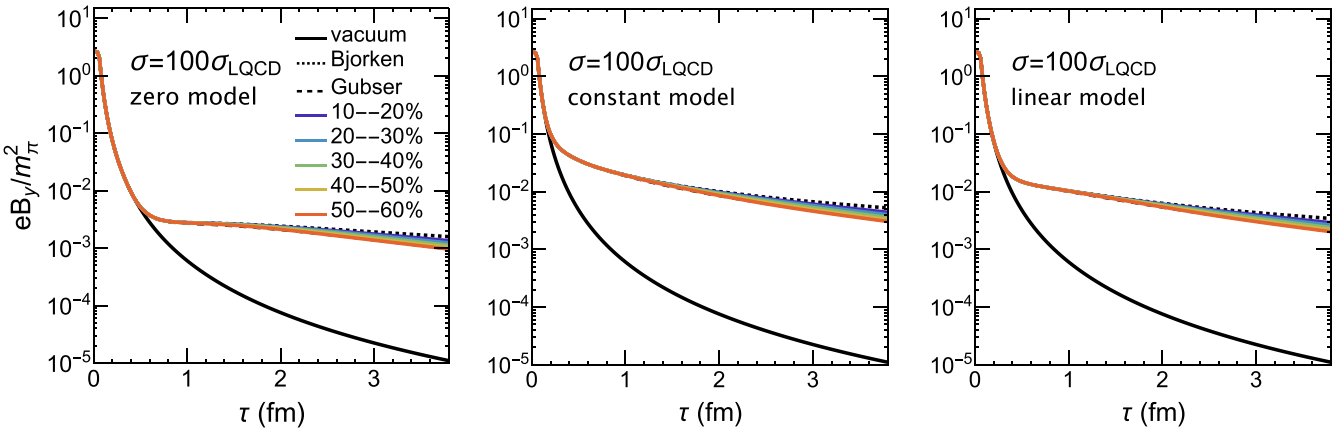

FIG. 6. Same as Fig. 5 but with hydro constant conductivity $\sigma = \sigma_{\rm LQCD}$.

TABLE II. Same as Table I but for constant conductivity $\sigma = \sigma_{\rm LQCD}$.

	a_0	b_0	b_1	b_2	c_0	c_1	c_2	c_3
zero model	−9.924	−2.145	−8.568	3.602	0.	14.76	12.063	14.417
constant model	−10.871	−1.786	−5.669	−7.969	0.0	10.273	16.761	20.953
linear model	−10.298	−2.785	−6.329	−1.854	0.0	16.528	10.082	18.5673

turn relies on a detailed understanding of the prethermal evolution (especially that of the quarks and antiquarks). From a phenomenological perspective, a magnetic field lifetime on the order of ≈ 1 fm/c in $\sqrt{s_{NN}} = 200$ GeV collisions appears to be needed for explaining relevant observables of the chiral magnetic effect and the $\Lambda/\bar{\Lambda}$ global polarization splitting [55–60]. According to our findings in this work, such a lifetime would suggest a considerable medium response contribution at the very early stage of the collisions. Whether this scenario could realistically occur will be an important question for future investigation.

Finally, while this work focuses on $\sqrt{s_{NN}} = 200$ GeV Au + Au collisions, our framework can be readily applied for other colliding systems at different collision energies. The simulation code for the static case has been made available at [61], and efforts are under way to make the full dynamical package publicly available in the future. Such a framework will allow quantitative estimates of many interesting observables induced by the dynamical magnetic fields in heavy ion collisions.

ACKNOWLEDGMENTS

The authors thank Dmitri E. Kharzeev for very helpful discussions at the early stage of this work. The research of A.H. is supported by the National Natural Science Foundation of China (NSFC) Grant No.12205309. A.H. and M.H. are supported by the Strategic Priority Research Program of Chinese Academy of Sciences Grant No. XDB34030000, the Fundamental Research Funds for the Central Universities, and the National Natural Science Foundation of China (NSFC) Grant No. 12235016. M.H. is also supported in part by the National Natural Science Foundation of China (NSFC) Grants No. 11725523, No. 11735007, and No. 12221005. D.S. is grateful for support by Key Laboratory of Quark and Lepton Physics Contract No. QLPL2022P01. J.L. acknowledges partial support by NSF Grant No. PHY-2209183 and the DOE-funded Beam Energy Scan Theory (BEST) Collaboration. S.S. is supported by the U.S. Department of Energy, Office of Science, Office of Nuclear Physics, Grants No. DE-FG88ER41450 and No. DE-SC0012704.

APPENDIX A: THE SOLUTIONS OF EQ. (11)

As mentioned before, we do not need to solve Eq. (11): it can be represented analytically by a boosted point charge. If we choose the distribution of protons in both projectile and target according to the Woods-Saxon distribution with the standard parameters [62],

$$\rho(r) = \rho_0 \frac{1 + w\left(\frac{r}{R}\right)^2}{1 + e^{\frac{r-R}{a}}}. \tag{A1}$$

For the Au nucleus, $a = 0.535$ fm, $R = 6.38$ fm, $w = 0$. In this work, we will use the Gauss theorem in the rest frame of the target, and then boost the electromagnetic fields to the laboratory frame with the velocity of the target. In the rest frame of the target,

$$\mathbf{E}_0 = \frac{e}{4\pi} Q(r_0) \frac{\mathbf{r}_0}{r_0^3}, \quad Q(r) = 4\pi \int_0^r \rho(x) x^2 dx,$$
$$\mathbf{B}_0 = 0, \quad \mathbf{r}_0 = \mathbf{x} - \mathbf{x}'. \tag{A2}$$

Where $\mathbf{x}$ and $\mathbf{x}'$ are the locations of the field and nucleus center respectively. After boosting to the laboratory frame,

$$\begin{aligned} E_x &= \gamma E_x^0, \quad & E_y &= \gamma E_y^0, \quad & E_z &= E_z^0, \\ B_x &= -\gamma\, v E_y^0, \quad & B_y &= \gamma\, v E_x^0, \quad & B_z &= 0. \end{aligned} \tag{A3}$$

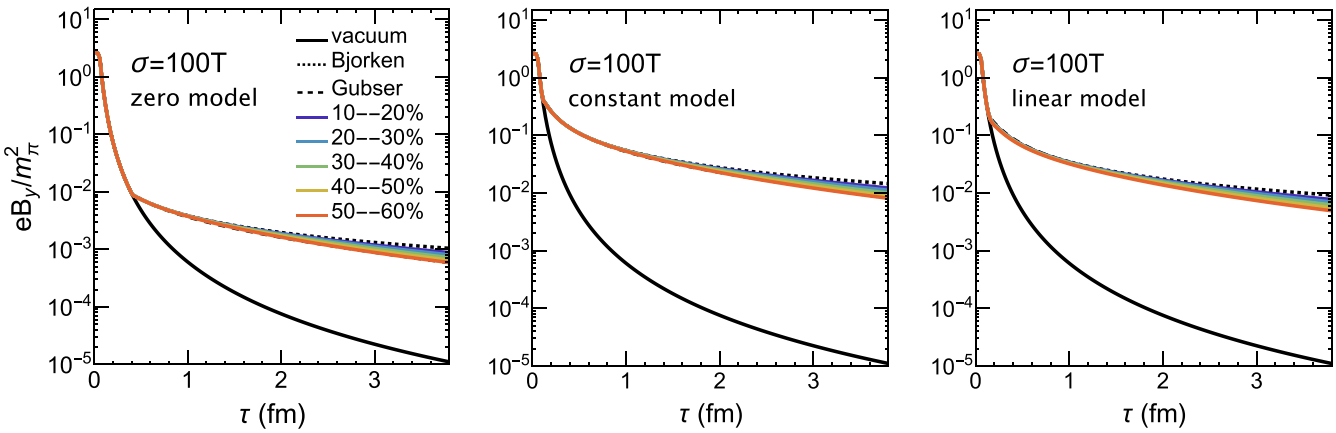

FIG. 7. Same as Fig. 5 but with hydro conductivity $\sigma = 100\,T$.

TABLE III. Same as Table I but for conductivity $\sigma = 100\,T$.

	a_0	b_0	b_1	b_2	c_0	c_1	c_2	c_3
zero model	−10.676	−4.081	−0.93	−18.58	0.052	19.787	13.497	14.866
constant model	−5.633	−1.344	−4.912	1.406	0	12.345	−0.039	0.677
linear model	−7.311	−1.248	0.483	−12.433	0	8.03	−0.223	16.904

The corresponding coordinates represented by the laboratory frame are

$$r_{0,x} = x - x', \quad r_{0,y} = y - y', \quad r_{0,z} = \gamma(z - z' - vt).$$

One can also generate the electromagnetic fields of heavy-ion collisions by using the Monte Carlo method as in the work of Deng and Huang [5]. In this work, we will use the above method for simplicity.

APPENDIX B: APPLYING YEE'S GRID ALGORITHM TO EQ. (12)

Yee's grid algorithm for Eq. (12) can be easily understood by the following representation:

$$\begin{aligned}
&\frac{dE_x}{dt}(t+dt/2, x+dx/2, y, z) = [\partial_y B_z - \partial_z B_y - \sigma\, E_x - \sigma_\chi B_x - \widetilde{J}_x]\big|(t+dt/2, x+dx/2, y, z),\\
&\frac{dE_y}{dt}(t+dt/2, x, y+dy/2, z) = [\partial_z B_x - \partial_x B_z - \sigma\, E_y - \sigma_\chi B_y - \widetilde{J}_y]\big|(t+dt/2, x, y+dy/2, z),\\
&\frac{dE_z}{dt}(t+dt/2, x, y, z+dz/2) = [\partial_x B_y - \partial_y B_x - \sigma\, E_z - \sigma_\chi B_z - \widetilde{J}_z]\big|(t+dt/2, x, y, z+dz/2),\\
&\frac{dB_x}{dt}(t, x, y+dy/2, z+dz/2) = [\partial_z E_y - \partial_y E_z]\big|(t, x, y+dy/2, z+dz/2),\\
&\frac{dB_y}{dt}(t, x+dx/2, y, z+dz/2) = [\partial_x E_z - \partial_z E_x]\big|(t, x+dx/2, y, z+dz/2),\\
&\frac{dB_z}{dt}(t, x+dx/2, y+dy/2, z) = [\partial_y E_x - \partial_x E_y]\big|(t, x+dx/2, y+dy/2, z).
\end{aligned} \tag{B1}$$

Let us use the center difference method at the given points to solve these equations. One can get the following results:

$$\begin{aligned}
E_x\big|^{n+1}_{i+1/2,j,k} &= E_x\big|^{n}_{i+1/2,j,k} + dt\,\frac{B_z\big|^{n+1/2}_{i+1/2,j+1/2,k} - B_z\big|^{n+1/2}_{i+1/2,j-1/2,k}}{dy} - dt\,\frac{B_y\big|^{n+1/2}_{i+1/2,j,k+1/2} - B_y\big|^{n+1/2}_{i+1/2,j,k-1/2}}{dz}\\
&\quad - dt\left\{\sigma\, E_x\big|^{n+1/2}_{i+1/2,j,k} + \sigma_\chi B_x\big|^{n+1/2}_{i+1/2,j,k} + \widetilde{J}_x\big|^{n+1/2}_{i+1/2,j,k}\right\},\\
E_y\big|^{n+1}_{i,j+1/2,k} &= E_y\big|^{n}_{i,j+1/2,k} + dt\,\frac{B_x\big|^{n+1/2}_{i,j+1/2,k+1/2} - B_x\big|^{n+1/2}_{i,j+1/2,k-1/2}}{dz} - dt\,\frac{B_z\big|^{n+1/2}_{i+1/2,j+1/2,k} - B_z\big|^{n+1/2}_{i-1/2,j+1/2,k}}{dx}\\
&\quad - dt\left\{\sigma\, E_y\big|^{n+1/2}_{i,j+1/2,k} + \sigma_\chi B_y\big|^{n+1/2}_{i,j+1/2,k} + \widetilde{J}_y\big|^{n+1/2}_{i,j+1/2,k}\right\},\\
E_z\big|^{n+1}_{i,j,k+1/2} &= E_z\big|^{n}_{i,j,k+1/2} + dt\,\frac{B_y\big|^{n+1/2}_{i+1/2,j,k+1/2} - B_y\big|^{n+1/2}_{i-1/2,j,k+1/2}}{dx} - dt\,\frac{B_x\big|^{n+1/2}_{i,j+1/2,k+1/2} - B_x\big|^{n+1/2}_{i,j-1/2,k+1/2}}{dy}\\
&\quad - dt\left\{\sigma\, E_z\big|^{n+1/2}_{i,j,k+1/2} + \sigma_\chi B_z\big|^{n+1/2}_{i,j,k+1/2} + \widetilde{J}_z\big|^{n+1/2}_{i,j,k+1/2}\right\};
\end{aligned} \tag{B2}$$

$$\begin{aligned}
B_x\big|^{n+1/2}_{i,j+1/2,k+1/2} &= B_x\big|^{n-1/2}_{i,j+1/2,k+1/2} + dt\left\{\frac{E_y\big|^{n}_{i,j+1/2,k+1} - E_y\big|^{n}_{i,j+1/2,k}}{dz} - \frac{E_z\big|^{n}_{i,j+1,k+1/2} - E_z\big|^{n}_{i,j,k+1/2}}{dy}\right\},\\
B_y\big|^{n+1/2}_{i+1/2,j,k+1/2} &= B_y\big|^{n-1/2}_{i+1/2,j,k+1/2} + dt\left\{\frac{E_z\big|^{n}_{i+1,j,k+1/2} - E_z\big|^{n}_{i,j,k+1/2}}{dx} - \frac{E_x\big|^{n}_{i+1/2,j+1,k+1} - E_x\big|^{n}_{i+1/2,j,k}}{dz}\right\},\\
B_z\big|^{n+1/2}_{i+1/2,j+1/2,k} &= B_z\big|^{n-1/2}_{i+1/2,j+1/2,k} + dt\left\{\frac{E_x\big|^{n}_{i+1/2,j+1,k} - E_x\big|^{n}_{i+1/2,j,k}}{dy} - \frac{E_y\big|^{n}_{i+1,j+1/2,k} - E_y\big|^{n}_{i,j+1/2,k}}{dx}\right\}.
\end{aligned} \tag{B3}$$

These two sets of equations should be further simplified for the next numerical simulations. Then the electric parts can be cast into the following:

$$
\begin{aligned}
E_x|^{n+1}_{i+1/2,j,k} =& COE|^{n+1/2}_{i+1/2,j,k} E_x|^{n}_{i+1/2,j,k} + CE|^{n+1/2}_{i+1/2,j,k}\Big[\frac{dt}{dy}\Big(B_z|^{n+1/2}_{i+1/2,j+1/2,k} - B_z|^{n+1/2}_{i+1/2,j-1/2,k}\Big) \\
&- \frac{dt}{dz}\Big(B_y|^{n+1/2}_{i+1/2,j,k+1/2} - B_y|^{n+1/2}_{i+1/2,j,k-1/2}\Big) - dt\sigma_\chi|^{n+1/2}_{i+1/2,j,k} B_x|^{n+1/2}_{i+1/2,j,k} - dt\widetilde{J}_x|^{n+1/2}_{i+1/2,j,k}\Big], \\
E_y|^{n+1}_{i,j+1/2,k} =& COE|^{n+1/2}_{i,j+1/2,k} E_y|^{n}_{i,j+1/2,k} + CE|^{n+1/2}_{i,j+1/2,k}\Big[\frac{dt}{dz}\Big(B_x|^{n+1/2}_{i,j+1/2,k+1/2} - B_x|^{n+1/2}_{i,j+1/2,k-1/2}\Big) \\
&- \frac{dt}{dx}\Big(B_z|^{n+1/2}_{i+1/2,j+1/2,k} - B_z|^{n+1/2}_{i-1/2,j+1/2,k}\Big) - dt\sigma_\chi|^{n+1/2}_{i,j+1/2,k} B_y|^{n+1/2}_{i,j+1/2,k} - dt\widetilde{J}_y|^{n+1/2}_{i,j+1/2,k}\Big], \\
E_z|^{n+1}_{i,j,k+1/2} =& COE|^{n+1/2}_{i,j,k+1/2} E_z|^{n}_{i,j,k+1/2} + CE|^{n+1/2}_{i,j,k+1/2}\Big[\frac{dt}{dx}\Big(B_y|^{n+1/2}_{i+1/2,j,k+1/2} - B_y|^{n+1/2}_{i-1/2,j,k+1/2}\Big) \\
&- \frac{dt}{dy}\Big(B_x|^{n+1/2}_{i,j+1/2,k+1/2} - B_x|^{n+1/2}_{i,j-1/2,k+1/2}\Big) - dt\sigma_\chi|^{n+1/2}_{i,j,k+1/2} B_z|^{n+1/2}_{i,j,k+1/2} - dt\widetilde{J}_z|^{n+1/2}_{i,j,k+1/2}\Big],
\end{aligned}
\tag{B4}
$$

where we have used an approximation $E_i|^{n+1/2} = (E_i|^{n+1} + E_i|^{n})/2$ for the term $\sigma\, E_i$, where $i = x, y, z$.

The magnetic field parts can be written as

$$
\begin{aligned}
B_x|^{n+1/2}_{i,j+1/2,k+1/2} =& B_x|^{n-1/2}_{i,j+1/2,k+1/2} + \frac{dt}{dz}\big(E_y|^{n}_{i,j+1/2,k+1} - E_y|^{n}_{i,j+1/2,k}\big) - \frac{dt}{dy}\big(E_z|^{n}_{i,j+1,k+1/2} - E_z|^{n}_{i,j,k+1/2}\big), \\
B_y|^{n+1/2}_{i+1/2,j,k+1/2} =& B_y|^{n-1/2}_{i+1/2,j,k+1/2} + \frac{dt}{dx}\big(E_z|^{n}_{i+1,j,k+1/2} - E_z|^{n}_{i,j,k+1/2}\big) - \frac{dt}{dz}\big(E_x|^{n}_{i+1/2,j,k+1} - E_x|^{n}_{i+1/2,j,k}\big), \\
B_z|^{n+1/2}_{i+1/2,j+1/2,k} =& B_z|^{n-1/2}_{i+1/2,j+1/2,k} + \frac{dt}{dy}\big(E_x|^{n}_{i+1/2,j+1,k} - E_x|^{n}_{i+1/2,j,k}\big) - \frac{dt}{dx}\big(E_y|^{n}_{i+1,j+1/2,k} - E_y|^{n}_{i,j+1/2,k}\big).
\end{aligned}
\tag{B5}
$$

First, the respective coordinates (n, i, j, k) denote $(t_0 + n\,dt, x_0 + i\,dx, y_0 + j\,dy, z_0 + k\,dz)$, where $n, i, j, k = 0, 1, 2, \ldots$. The coefficients are

$$
CE|^{n}_{i,j,k} = \frac{2}{2 + dt\,\sigma|^{n}_{i,j,k}}, \quad COE|^{n}_{i,j,k} = \frac{2 - dt\,\sigma|^{n}_{i,j,k}}{2 + dt\,\sigma|^{n}_{i,j,k}},
\tag{B6}
$$

in which $\sigma|^{n}_{i,j,k} = \sigma(t_0 + n\,dt, x_0 + i\,dx, y_0 + j\,dy, z_0 + k\,dz)$.

Second, the external source terms are

$$
\widetilde{J}_m|^{n}_{i,j,k} = \sigma|^{n}_{i,j,k} E^{ext}_m|^{n}_{i,j,k} + \sigma_\chi|^{n}_{i,j,k} B^{ext}_m|^{n}_{i,j,k}, \quad m = (x, y, z).
\tag{B7}
$$

Finally, the coordinates of the magnetic field at the chiral magnetic effect term in the set of equations (B4) are not the same as the positions of the computed magnetic field. So we need to represent them with the computed magnetic field. There is one method to solve this problem, i.e.,

$$
\begin{aligned}
B_x|^{n+1/2}_{i+1/2,j,k} =& \tfrac{1}{8}\big(B_x|^{n+1/2}_{i+1,j+1/2,k+1/2} + B_x|^{n+1/2}_{i+1,j+1/2,k-1/2} + B_x|^{n+1/2}_{i+1,j-1/2,k+1/2} + B_x|^{n+1/2}_{i+1,j-1/2,k-1/2} \\
&\times B_x|^{n+1/2}_{i,j+1/2,k+1/2} + B_x|^{n+1/2}_{i,j+1/2,k-1/2} + B_x|^{n+1/2}_{i,j-1/2,k+1/2} + B_x|^{n+1/2}_{i,j-1/2,k-1/2}\big), \\
B_y|^{n+1/2}_{i,j+1/2,k} =& \tfrac{1}{8}\big(B_y|^{n+1/2}_{i+1/2,j+1,k+1/2} + B_y|^{n+1/2}_{i+1/2,j+1,k-1/2} + B_y|^{n+1/2}_{i-1/2,j+1,k+1/2} + B_y|^{n+1/2}_{i-1/2,j+1,k-1/2} \\
&\times B_y|^{n+1/2}_{i+1/2,j,k+1/2} + B_y|^{n+1/2}_{i+1/2,j,k-1/2} + B_y|^{n+1/2}_{i-1/2,j,k+1/2} + B_y|^{n+1/2}_{i-1/2,j,k-1/2}\big), \\
B_z|^{n+1/2}_{i,j,k+1/2} =& \tfrac{1}{8}\big(B_z|^{n+1/2}_{i+1/2,j+1/2,k+1} + B_z|^{n+1/2}_{i+1/2,j-1/2,k+1} + B_z|^{n+1/2}_{i-1/2,j+1/2,k+1} + B_z|^{n+1/2}_{i-1/2,j-1/2,k+1} \\
&\times B_z|^{n+1/2}_{i+1/2,j+1/2,k} + B_z|^{n+1/2}_{i+1/2,j-1/2,k} + B_z|^{n+1/2}_{i-1/2,j+1/2,k} + B_z|^{n+1/2}_{i-1/2,j-1/2,k}\big).
\end{aligned}
\tag{B8}
$$

APPENDIX C: LEVI-CIVITA TENSOR AND ELECTROMAGNETIC TENSOR IN MILNE SPACE

In Milne coordinates, the Levi-Civita tensor is different from that in Minkowski coordinates,

$$\epsilon^{\mu\nu\rho\sigma} = \frac{1}{\sqrt{|g|}}\widetilde{\epsilon}^{\mu\nu\rho\sigma}, \quad \epsilon_{\mu\nu\rho\sigma} = \theta(g)\sqrt{|g|}\widetilde{\epsilon}_{\mu\nu\rho\sigma}, \tag{C1}$$

where $g = \det(g_{\mu\nu})$, θ is the Heaviside step function, and the Levi-Civita symbol in the Minkowski coordinate $\widetilde{\epsilon}^{\mu\nu\rho\sigma}$ is defined by the following,

$$\widetilde{\epsilon}^{\mu\nu\rho\sigma} = \widetilde{\epsilon}_{\mu\nu\rho\sigma} = \begin{cases} +1, & \text{even permutation of } (0, 1, 2, \ldots, n-1), \\ -1, & \text{odd permutation of } (0, 1, 2, \ldots, n-1), \\ 0, & \text{otherwise.} \end{cases}$$

Taking $g = -\tau^2$ and $|g| = \tau^2$, one finds $\epsilon^{0123} = \frac{1}{\tau}$ and $\epsilon_{0123} = -\tau$.

The electric and magnetic fields in the Milne space are defined by

$$\widetilde{E}^i = F_M^{i0}, \quad \widetilde{B}^i = \widetilde{F}_M^{i0}. \tag{C2}$$

Then one can directly derive the electromagnetic tensor in Milne space with the above Levi-Civita definition, which can be expressed as

$$F_M^{\mu\nu} = \begin{pmatrix} 0 & -\widetilde{E}^x & -\widetilde{E}^y & -\widetilde{E}^\eta \\ \widetilde{E}^x & 0 & -\tau\,\widetilde{B}^\eta & \frac{\widetilde{B}^y}{\tau} \\ \widetilde{E}^y & \tau\,\widetilde{B}^\eta & 0 & -\frac{\widetilde{B}^x}{\tau} \\ \widetilde{E}^\eta & -\frac{\widetilde{B}^y}{\tau} & \frac{\widetilde{B}^x}{\tau} & 0 \end{pmatrix}, \quad \widetilde{F}_M^{\mu\nu} = \begin{pmatrix} 0 & -\widetilde{B}^x & -\widetilde{B}^y & -\widetilde{B}^\eta \\ \widetilde{B}^x & 0 & \tau\,\widetilde{E}^\eta & -\frac{\widetilde{E}^y}{\tau} \\ \widetilde{B}^y & -\tau\,\widetilde{E}^\eta & 0 & \frac{\widetilde{E}^x}{\tau} \\ \widetilde{B}^\eta & \frac{\widetilde{E}^y}{\tau} & -\frac{\widetilde{E}^x}{\tau} & 0 \end{pmatrix} \tag{C3}$$

APPENDIX D: THE VELOCITY IN MILNE SPACE AND MINKOWSKI SPACE

We will need some simplified velocities of the medium when we do the numerical calculations in the moving medium for doing comparisons, such as the static velocity, Bjorken velocity, and Gubser velocity. These velocities in the Milne space and Minkowski coordinates can be expressed as follows:

$$u_M^\mu = R^\mu_{\ \nu} u^\nu = \begin{cases} \left(\cosh\eta, 0, 0, -\dfrac{\sinh\eta}{\tau}\right) & \text{for static case: } u^\mu = (1, 0, 0, 0), \\ (1, 0, 0, 0), & \text{for Bjorken flow: } u^\mu = \left(\dfrac{t}{\tau}, 0, 0, \dfrac{z}{\tau}\right), \\ \left(u^\tau, u^\perp \dfrac{x}{x_\perp}, u^\perp \dfrac{y}{x_\perp}, 0\right), & \text{for Gubser flow: } u^\mu = \left(u^\tau\,\cosh\eta, u^\perp \dfrac{x}{x_\perp}, u^\perp \dfrac{y}{x_\perp}, u^\tau\,\sinh\eta\right). \end{cases} \tag{D1}$$

The velocity with M subscript represents the velocity in Milne coordinates, while the velocity without M subscript is the velocity in Minkowski coordinates. The transformation matrix and antitransformation matrix from Minkowski coordinates to Milne space are defined as follows:

$$R^\mu_{\ \nu} = \frac{\partial\, x_M^\mu}{\partial\, x^\nu} = \begin{bmatrix} \cosh\eta & 0 & 0 & -\sinh\eta \\ 0 & 1 & 0 & 0 \\ 0 & 0 & 1 & 0 \\ -\frac{\sinh\eta}{\tau} & 0 & 0 & \frac{\cosh\eta}{\tau} \end{bmatrix}, \quad \check{R}^\mu_{\ \nu} = \frac{\partial\, x^\mu}{\partial\, x_M^\nu} = \begin{bmatrix} \cosh\eta & 0 & 0 & \tau\sinh\eta \\ 0 & 1 & 0 & 0 \\ 0 & 0 & 1 & 0 \\ \sinh\eta & 0 & 0 & \tau\cosh\eta \end{bmatrix}. \tag{D2}$$

The corresponding components in the velocity of the Gubser flow are expressed as [63,64]

$$u^\tau = \frac{1 + q^2\tau^2 + q^2x_\perp^2}{2q\tau\sqrt{1+g^2}}, \quad u^\perp = \frac{qx_\perp}{\sqrt{1+g^2}}, \quad g = \frac{1 + q^2x_\perp^2 - q^2\tau^2}{2q\tau}. \tag{D3}$$

Herein the proper time is defined by $\tau = \sqrt{t^2 - z^2}$ and the transverse distance $x_\perp = \sqrt{x^2 + y^2}$, while the temperature in the local rest frame of the fluid is defined as

$$T = \frac{1}{\tau\, f_*^{1/4}}\left(\frac{\hat{T}_0}{(1+g^2)^{1/3}} + \frac{H_0 g}{\sqrt{1+g^2}}\left[1 - (1+g^2)^{1/6}\,{}_2F_1\left(\frac{1}{2}, \frac{1}{6}; \frac{3}{2}; -g^2\right)\right]\right). \tag{D4}$$

$\hat{T}_0$ is a dimensionless integration constant, and $f_* = \epsilon/T^4 = 11$, $q = 1/(4.3\text{ fm})$. For RHIC energy $\sqrt{s_{NN}} = 200$ GeV, $\hat{T}_0 = 5.55$ and $H_0 = 0.33$. The function ${}_2F_1$ denotes a hypergeometric function.

For the Bjorken flow, the temperature changes as

$$T(\tau) = T_0 \frac{\tau_0}{\tau}, \tag{D5}$$

where the T_0 is the temperature at time τ_0, which can be given by the Glauber model. For example, $T_0 \approx 400$ MeV at the center of the QGP at $\tau_0 = 0.4$ fm for $\sqrt{s_{NN}} = 200$ GeV Au + Au collisions.

[1] D. E. Kharzeev, L. D. McLerran, and H. J. Warringa, The Effects of topological charge change in heavy ion collisions: "Event by event $\mathcal{P}$ and $\mathcal{CP}$ violation", Nucl. Phys. A **803**, 227 (2008).

[2] V. Skokov, A. Yu. Illarionov, and V. Toneev, Estimate of the magnetic field strength in heavy-ion collisions, Int. J. Mod. Phys. A **24**, 5925 (2009).

[3] V. Voronyuk, V. D. Toneev, W. Cassing, E. L. Bratkovskaya, V. P. Konchakovski, and S. A. Voloshin, Electromagnetic field evolution in relativistic heavy-ion collisions, Phys. Rev. C **83**, 054911 (2011).

[4] A. Bzdak and V. Skokov, Event-by-event fluctuations of magnetic and electric fields in heavy ion collisions, Phys. Lett. B **710**, 171 (2012).

[5] W.-T. Deng and X.-G. Huang, Event-by-event generation of electromagnetic fields in heavy-ion collisions, Phys. Rev. C **85**, 044907 (2012).

[6] J. Bloczynski, X.-G. Huang, X. Zhang, and J. Liao, Azimuthally fluctuating magnetic field and its impacts on observables in heavy-ion collisions, Phys. Lett. B **718**, 1529 (2013).

[7] L. McLerran and V. Skokov, Comments about the electromagnetic field in heavy-ion collisions, Nucl. Phys. A **929**, 184 (2014).

[8] K. Tuchin, Initial value problem for magnetic fields in heavy ion collisions, Phys. Rev. C **93**, 014905 (2016).

[9] Y. Chen, X.-L. Sheng, and G.-L. Ma, Electromagnetic fields from the extended Kharzeev-McLerran-Warringa model in relativistic heavy-ion collisions, Nucl. Phys. A **1011**, 122199 (2021).

[10] D. E. Kharzeev, K. Landsteiner, A. Schmitt, and H.-U. Yee, Strongly Interacting Matter in Magnetic Fields: A Guide to This Volume, *in Strongly Interacting Matter in Magnetic Fields, Lecture Notes in Physics* Vol. 871 (Springer, Berlin, 2013), p. 1.

[11] D. E. Kharzeev, J. Liao, S. A. Voloshin, and G. Wang, Chiral magnetic and vortical effects in high-energy nuclear collisions—A status report, Prog. Part. Nucl. Phys. **88**, 1 (2016).

[12] D. E. Kharzeev and J. Liao, Chiral magnetic effect reveals the topology of gauge fields in heavy-ion collisions, Nat. Rev. Phys. **3**, 55 (2021).

[13] K. Fukushima, Extreme matter in electromagnetic fields and rotation, Prog. Part. Nucl. Phys. **107**, 167 (2019).

[14] I. A. Shovkovy, Anomalous plasma: Chiral magnetic effect and all that, in *Peter Suranyi 87th Birthday Festschrift* (World Scientific, Singapore, 2022), p. 291.

[15] W. Li and G. Wang, Chiral magnetic effects in nuclear collisions, Annu. Rev. Nucl. Part. Sci. **70**, 293 (2020).

[16] X.-G. Huang, Electromagnetic fields and anomalous transports in heavy-ion collisions–A pedagogical review, Rep. Prog. Phys. **79**, 076302 (2016).

[17] S. Gupta, The electrical conductivity and soft photon emissivity of the QCD plasma, Phys. Lett. B **597**, 57 (2004).

[18] G. Aarts, C. Allton, J. Foley, S. Hands, and S. Kim, Spectral Functions at Small Energies and the Electrical Conductivity in Hot Quenched Lattice QCD, Phys. Rev. Lett. **99**, 022002 (2007).

[19] H. T. Ding, A. Francis, O. Kaczmarek, F. Karsch, E. Laermann, and W. Soeldner, Thermal dilepton rate and electrical conductivity: An analysis of vector current correlation functions in quenched lattice QCD, Phys. Rev. D **83**, 034504 (2011).

[20] H.-T. Ding, O. Kaczmarek, and F. Meyer, Thermal dilepton rates and electrical conductivity of the QGP from the lattice, Phys. Rev. D **94**, 034504 (2016).

[21] G. Aarts and J. M. Martinez Resco, Ward identity and electrical conductivity in hot QED, J. High Energy Phys. 11 (2002) 022.

[22] X.-G. Huang and J. Liao, Axial Current Generation from Electric Field: Chiral Electric Separation Effect, Phys. Rev. Lett. **110**, 232302 (2013).

[23] Y. Jiang, X.-G. Huang, and J. Liao, Chiral electric separation effect in the quark-gluon plasma, Phys. Rev. D **91**, 045001 (2015).

[24] V. M. Bannur, Self-consistent quasiparticle model for quark-gluon plasma, Phys. Rev. C **75**, 044905 (2007).

[25] A. Das, H. Mishra, and R. K. Mohapatra, Electrical conductivity and Hall conductivity of a hot and dense hadron gas in a magnetic field: A relaxation time approach, Phys. Rev. D **99**, 094031 (2019).

[26] A. Hosoya and K. Kajantie, Transport coefficients of QCD matter, Nucl. Phys. B **250**, 666 (1985).

[27] S.-I. Nam, Electrical conductivity of quark matter at finite T under external magnetic field, Phys. Rev. D **86**, 033014 (2012).

[28] W. Cassing, O. Linnyk, T. Steinert, and V. Ozvenchuk, Electrical Conductivity of Hot QCD Matter, Phys. Rev. Lett. **110**, 182301 (2013).

[29] P. B. Arnold, G. D. Moore, and L. G. Yaffe, Transport coefficients in high temperature gauge theories. 2. Beyond leading log, J. High Energy Phys. 05 (2003) 051.

[30] Z. Wang, J. Zhao, C. Greiner, Z. Xu, and P. Zhuang, Incomplete electromagnetic response of hot QCD matter, Phys. Rev. C **105**, L041901 (2022).

[31] V. Roy, S. Pu, L. Rezzolla, and D. Rischke, Analytic Bjorken flow in one-dimensional relativistic magnetohydrodynamics, Phys. Lett. B **750**, 45 (2015).

[32] S. Pu, V. Roy, L. Rezzolla, and D. H. Rischke, Bjorken flow in one-dimensional relativistic magnetohydrodynamics with magnetization, Phys. Rev. D **93**, 074022 (2016).

[33] G. Inghirami, L. Del Zanna, A. Beraudo, M. H. Moghaddam, F. Becattini, and M. Bleicher, Numerical magneto-hydrodynamics for relativistic nuclear collisions, Eur. Phys. J. C **76**, 659 (2016).

[34] G. Inghirami, M. Mace, Y. Hirono, L. Del Zanna, D. E. Kharzeev, and M. Bleicher, Magnetic fields in heavy ion collisions: flow and charge transport, Eur. Phys. J. C **80**, 293 (2020).

[35] K. Tuchin, Electromagnetic field and the chiral magnetic effect in the quark-gluon plasma, Phys. Rev. C **91**, 064902 (2015).

[36] E. Stewart and K. Tuchin, Magnetic field in expanding quark-gluon plasma, Phys. Rev. C **97**, 044906 (2018).
[37] E. Stewart and K. Tuchin, Continuous evolution of electromagnetic field in heavy-ion collisions, Nucl. Phys. A **1016**, 122308 (2021).
[38] U. Gürsoy, D. Kharzeev, and K. Rajagopal, Magnetohydrodynamics, charged currents and directed flow in heavy ion collisions, Phys. Rev. C **89**, 054905 (2014).
[39] U. Gürsoy, D. Kharzeev, E. Marcus, K. Rajagopal, and C. Shen, Charge-dependent flow induced by magnetic and electric fields in heavy ion collisions, Phys. Rev. C **98**, 055201 (2018).
[40] H. Li, X.-L. Sheng, and Q. Wang, Electromagnetic fields with electric and chiral magnetic conductivities in heavy ion collisions, Phys. Rev. C **94**, 044903 (2016).
[41] B. G. Zakharov, Electromagnetic response of quark–gluon plasma in heavy-ion collisions, Phys. Lett. B **737**, 262 (2014).
[42] A. Amato, G. Aarts, C. Allton, P. Giudice, S. Hands, and J.-I. Skullerud, Transport coefficients of the QGP, PoS **LATTICE2013**, 176 (2014).
[43] K. Yee, Numerical solution of initial boundary value problems involving Maxwell's equations in isotropic media, IEEE Trans. Antennas Propag. **14**, 302 (1966).
[44] https://github.com/brangja/EB-in-HIC.git.
[45] D. E. Kharzeev and H. J. Warringa, Chiral magnetic conductivity, Phys. Rev. D **80**, 034028 (2009).
[46] L. Thakur, P. K. Srivastava, G. P. Kadam, M. George, and H. Mishra, Shear viscosity η to electrical conductivity σ_{el} ratio for an anisotropic QGP, Phys. Rev. D **95**, 096009 (2017).
[47] G. P. Kadam, H. Mishra, and L. Thakur, Electrical and thermal conductivities of hot and dense hadronic matter, Phys. Rev. D **98**, 114001 (2018).
[48] L. Thakur and P. K. Srivastava, Electrical conductivity of a hot and dense QGP medium in a magnetic field, Phys. Rev. D **100**, 076016 (2019).
[49] A. Das, H. Mishra, and R. K. Mohapatra, Electrical conductivity and Hall conductivity of a hot and dense quark gluon plasma in a magnetic field: A quasiparticle approach, Phys. Rev. D **101**, 034027 (2020).
[50] M. Greif, I. Bouras, C. Greiner, and Z. Xu, Electric conductivity of the quark-gluon plasma investigated using a perturbative QCD based parton cascade, Phys. Rev. D **90**, 094014 (2014).
[51] C. Gale, S. Jeon, and B. Schenke, Hydrodynamic modeling of heavy-ion collisions, Int. J. Mod. Phys. A **28**, 1340011 (2013).
[52] B. Schenke, S. Jeon, and C. Gale, Elliptic and Triangular Flow in Event-by-Event (3+1)D Viscous Hydrodynamics, Phys. Rev. Lett. **106**, 042301 (2011).
[53] B. Schenke, S. Jeon, and C. Gale, (3+1)D hydrodynamic simulation of relativistic heavy-ion collisions, Phys. Rev. C **82**, 014903 (2010).
[54] S. McDonald, C. Shen, F. Fillion-Gourdeau, S. Jeon, and C. Gale, Hydrodynamic predictions for Pb+Pb collisions at 5.02 TeV, Phys. Rev. C **95**, 064913 (2017).
[55] B. Müller and A. Schäfer, Chiral magnetic effect and an experimental bound on the late time magnetic field strength, Phys. Rev. D **98**, 071902(R) (2018).
[56] X. Guo, J. Liao, and E. Wang, Spin hydrodynamic generation in the charged subatomic swirl, Sci. Rep. **10**, 2196 (2020).
[57] Y. Guo, S. Shi, S. Feng, and J. Liao, Magnetic field induced polarization difference between hyperons and anti-hyperons, Phys. Lett. B **798**, 134929 (2019).
[58] S. Shi, Y. Jiang, E. Lilleskov, and J. Liao, Anomalous chiral transport in heavy ion collisions from anomalous-viscous fluid dynamics, Ann. Phys. (NY) **394**, 50 (2018).
[59] S. Shi, H. Zhang, D. Hou, and J. Liao, Signatures of Chiral Magnetic Effect in the Collisions of Isobars, Phys. Rev. Lett. **125**, 242301 (2020).
[60] K. Xu, F. Lin, A. Huang, and M. Huang, $\Lambda/\bar{\Lambda}$ polarization and splitting induced by rotation and magnetic field, Phys. Rev. D **106**, L071502 (2022).
[61] https://github.com/brangja/EB-in-HIC.git.
[62] B. Alver, M. Baker, C. Loizides, and P. Steinberg, The PHOBOS Glauber Monte Carlo, arXiv:0805.4411.
[63] S. S. Gubser, Symmetry constraints on generalizations of Bjorken flow, Phys. Rev. D **82**, 085027 (2010).
[64] S. S. Gubser and A. Yarom, Conformal hydrodynamics in Minkowski and de Sitter spacetimes, Nucl. Phys. B **846**, 469 (2011).